Volcanic ash, victims, and tsunami debris from the Late Bronze Age Thera eruption discovered at Çeşme-Bağlararası (Turkey)

Vasıf Şahoğlu[a,2,1], Johannes H. Sterba[b], Timor Katz[c], Ümit Çayır[d], Ümit Gündoğan[e], Natalia Tyuleneva[f], İrfan Tuğcu[g], Max Bichler[b], Hayat Erkanal[a,3], and Beverly N. Goodman-Tchernov[f,1,2]

[a]Department of Archaeology, Ankara University Mustafa V. Koç Research Center for Maritime Archaeology, Ankara University, Ankara 06100, Turkey; [b]Center for Labelling and Isotope Production, TRIGA (Training, Research, Isotopes, General Atomics) Center Atominstitut, Technische Universität Wien, Wien 1020, Austria; [c]Israel Oceanographic and Limnological Research, Shikmona 31080, Israel; [d]Department of Archaeology, Sivas Cumhuriyet University, Sivas 58140, Turkey; [e]Department of Archaeology, Batman University, Batman 72100, Turkey; [f]Charney School of Marine Sciences, Department of Marine Geosciences, University of Haifa, Mt. Carmel 31905, Israel; and [g]Department of Archaeology, Osmaniye Korkut Ata University, Osmaniye 80000, Turkey

Edited by Mehmet Özdoğan, Department of Archaeology and Art History, Istanbul Universitesi, Istanbul, Turkey; received August 13, 2021; accepted November 16, 2021

The Late Bronze Age Thera eruption was one of the largest natural disasters witnessed in human history. Its impact, consequences, and timing have dominated the discourse of ancient Mediterranean studies for nearly a century. Despite the eruption's high intensity (Volcanic Explosivity Index 7; Dense Rock Equivalent of 78 to 86 km) [T. H. Druitt, F. W. McCoy, G. E. Vougioukalakis, *Elements* 15, 185–190 (2019)] and tsunami-generating capabilities [K. Minoura *et al.*, *Geology* 28, 59–62 (2000)], few tsunami deposits are reported. In contrast, descriptions of pumice, ash, and tephra deposits are widely published. This mismatch may be an artifact of interpretive capabilities, given how rapidly tsunami sedimentology has advanced in recent years. A well-preserved volcanic ash layer and chaotic destruction horizon were identified in stratified deposits at Çeşme-Bağlararası, a western Anatolian/Aegean coastal archaeological site. To interpret these deposits, archaeological and sedimentological analysis (X-ray fluorescence spectroscopy instrumental neutron activation analysis, granulometry, micropaleontology, and radiocarbon dating) were performed. According to the results, the archaeological site was hit by a series of strong tsunamis that caused damage and erosion, leaving behind a thick layer of debris, distinguishable by its physical, biological, and chemical signature. An articulated human and dog skeleton discovered within the tsunami debris are in situ victims related to the Late Bronze Age Thera eruption event. Calibrated radiocarbon ages from well-constrained, short-lived organics from within the tsunami deposit constrain the event to no earlier than 1612 BCE. The deposit provides a time capsule that demonstrates the nature, enormity, and expansive geographic extent of this catastrophic event.

tsunami | volcanic ash | Minoan | geoarchaeology | Aegean

The Late Bronze Age (LBA) eruption of Thera on the Island of Santorini was a pivotal event for the Mediterranean and the world (1–3). Loss of life and property damage related to the eruption, including earthquakes, pyroclastic debris flow and ash, and tsunami landfall affected the entire region (4, 5) (Fig. 1). It has been proposed that climatic responses were felt for decades afterward (6). Polar archives (7) and distant tree-ring records (8, 9) also reflect the event. Debate exists regarding its role in the end of Minoan cultural dominance, particularly with regard to seafaring settlements (10). It is commonly used as a tephrochronological marker to interrelate stratigraphic sequences (11, 12).

Despite the massive size of the event, remains from human victims have never been reported, even in the heavily impacted near-field site of Akrotiri (13). Some scholars argue that initial, precursory volcanic activity drove residents to evacuate the island, though many may have been incinerated at sea in pyroclastic density flows (14, 15). There were at least some surviving refugees, as is evident from the arrival of Thera-type architecture and cultural materials elsewhere postevent (16).

According to archaeological correlations, the event occurred during the Late Minoan IA Period (17, 18), which is contemporaneous with the 18th Egyptian Dynasty in the 16th century BCE (19). This range of dates is termed the "low chronology." However, measurements from radiocarbon dating of olive wood from the ash layers at Santorini have produced older ages, primarily in the mid-late 17th century BCE, a range of dates referred to as the "high chronology" (20–22). This mismatch upsets the understanding of which people, what powers, and related events coexisted at that time (10, 23, 24).

Significance

The significance of this study is multi-faceted, touching upon methodological advances in multidisciplinary approaches (earth sciences/geology–archaeology) as well as contributing to the historical and chronological understanding of the Late Bronze Age Thera eruption impacts. Our study presents physical evidence that very large, damaging tsunamis arrived even in the northern Aegean, an area previously assumed to be affected only by ash fallout. The tsunami deposits at Çeşme-Bağlararası contain the first victims (human and dog) ever identified related to the eruption and its immediate consequences. The work also introduces nine radiocarbon ages directly from the event deposit that will be of great interest and cause significant discussion amongst scholars, particularly given their context within a well-constrained, undisturbed, stratigraphic archaeological sequence.

Author contributions: V.Ş., J.H.S., and B.N.G.-T. designed research; V.Ş., J.H.S., T.K., U.C., U.G., N.T., İ.T., M.B., H.E., and B.N.G.-T. performed research; V.Ş., J.H.S., T.K., İ.T., M.B., and B.N.G.-T. contributed new reagents/analytic tools; V.Ş., J.H.S., T.K., N.T., and B.N.G.-T. analyzed data; and V.Ş., J.H.S., T.K., and B.N.G.-T. wrote the paper.

The authors declare no competing interest.

This article is a PNAS Direct Submission.

[1]V.Ş. and B.N.G.-T. contributed equally to this work.

[2]To whom correspondence may be addressed. Email: bgoodman@univ.haifa.ac.il or sahoglu@ankara.edu.tr.

[3]Deceased 28 July 2019.

This article contains supporting information online at http://www.pnas.org/lookup/suppl/doi:10.1073/pnas.2114213118/-/DCSupplemental.

Published December 27, 2021.

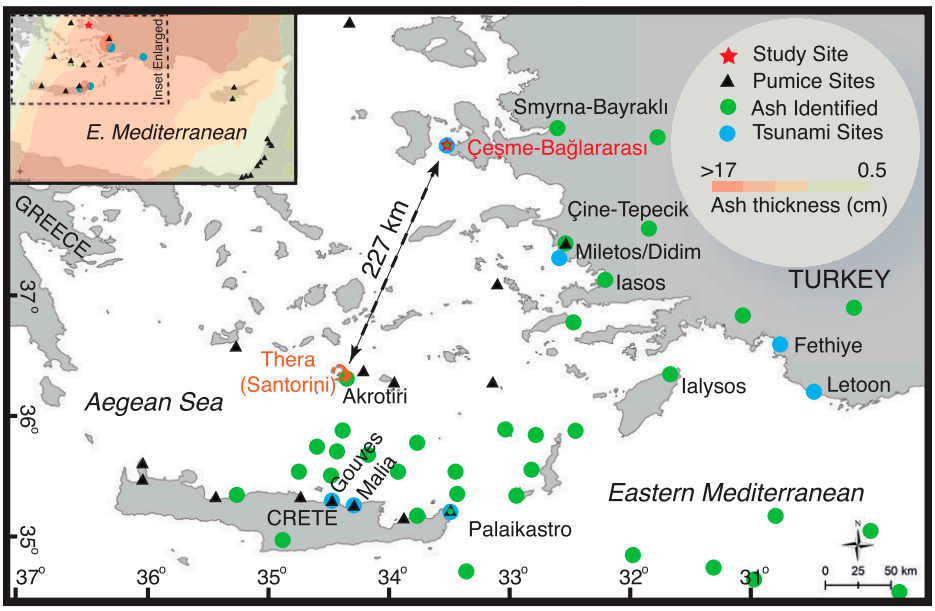

Fig. 1. Map of the Aegean and Eastern Mediterranean Seas, highlighting locations with evidence related to the LBA eruption of Thera ("Bo") (11–15, 50, 57–59). The *Inset* map shows ash thickness contours (57).

Çeşme-Bağlararası (Fig. 1) was occupied near-continuously at least from the mid third millennium BCE until the 13th century BCE (25, 26). The site was a thriving western Anatolian coastal settlement with evidence for land and sea trade, including Minoan cultural elements during the first half of the second millennium BCE. Given its location and complexity, it would have been a central regional hub (26). Today, the site is located about 200 m from the modern Çeşme Bay coastline and marina. Paleogeographic reconstructions from the LBA place the waterline even closer (<100 m) and include east- and west-oriented rivers flanking the site (27). Estimates of relative sea level between 3,000 and 4,000 y ago are within a meter of modern values (including error) (28), and observations of the elevation relationship between architectural components of the site and the coastal water table (sweetwater) suggest similarity to today. Combined, this suggests that while relative sea level may be similar today, the coastal positioning has changed.

Beginning in 2009, excavations shifted to an area that was already deserted at the time of the Theran eruption. This area included massive fortification walls that were heavily disturbed with a laterally extensive layer of rubble and chaotic sediments, including a distinctive ash and a charred layer (Fig. 2 and *SI Appendix*, Fig. S1). A representative sedimentological section was analyzed using multiple proxy methodologies (*Materials and Methods*) to determine the source, age, transportation mechanisms, and taphonomic history of the sediments, which was then compared to the finds from the archaeological excavation.

Results

General Description of the Sedimentological Horizons. Three main sequences, H1, H2, and H3, were identified (Figs. 3 and 4), and the lowermost H1 subdivided into four subphases (H1a through d). The base of the sequence (H1a) contains framework-supported large rubble (~25 to 40 cm), pottery (CB Level 1, which includes Late Minoan IA [LM1A] Cretan and minoanizing pottery), shell, and bone. This is followed by similar but matrix-supported sediments without bedding, a fine, noncontinuous ash layer (<1 cm, top of H1a; Fig. 3), imbricated inclusions, and smaller rubble pieces. After the broken ash layer, another sequence (H1b) with the same chaotic characteristics repeats and are topped by a thicker ash layer at an elevation of +0.62 msl (top of H1b; Fig. 3). Elemental values of the ash match tephra from the Santorini "Bo" eruption (*SI Appendix*, Fig. S5). The radiocarbon ages of two samples from above and two samples from below the layer are in the range of both low and high chronologies (Fig. 3 and *SI Appendix*, Figs. S6–S8). The lower contact of the H1b ash layer is sharp, and the upper contact has truncated flame-like structures. An approximately 8-cm-thick layer (H1c) above the ash contains similar sediments and inclusions as H1b; however, instead of another ash layer, it ends with a distinctive, charcoal-rich lens with charred remains. In H1d (Fig. 3), there is a repeat of similar sediments, inclusions, and pottery (CB Level 1, which includes LM1A Cretan and minoanizing pottery) but with the addition of larger rubble (~<15-cm diameter) capped by imbricated pebbles and a very fine (~1 cm) terminal silty layer lens ("mudcap," Fig. 4).

Marine Markers and Elemental Values in the Sedimentological Horizons. The H1a through d sequence has an overall average foraminifera abundance of approximately five to nine

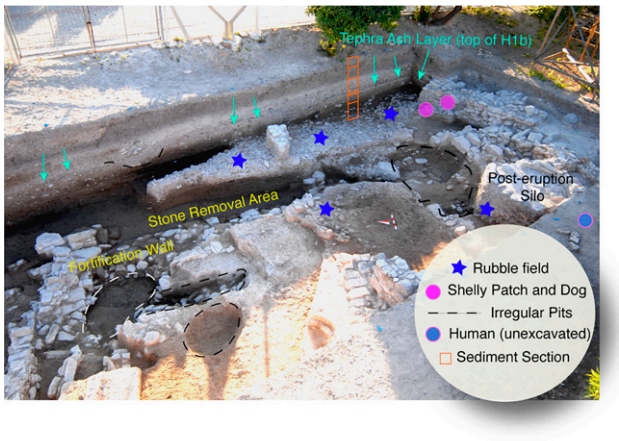

Fig. 2. Çeşme-Bağlararası Excavation. Photograph showing the site as it appeared in 2012. Features from the damaged and disrupted area as well as locations of sediment sampling are highlighted.

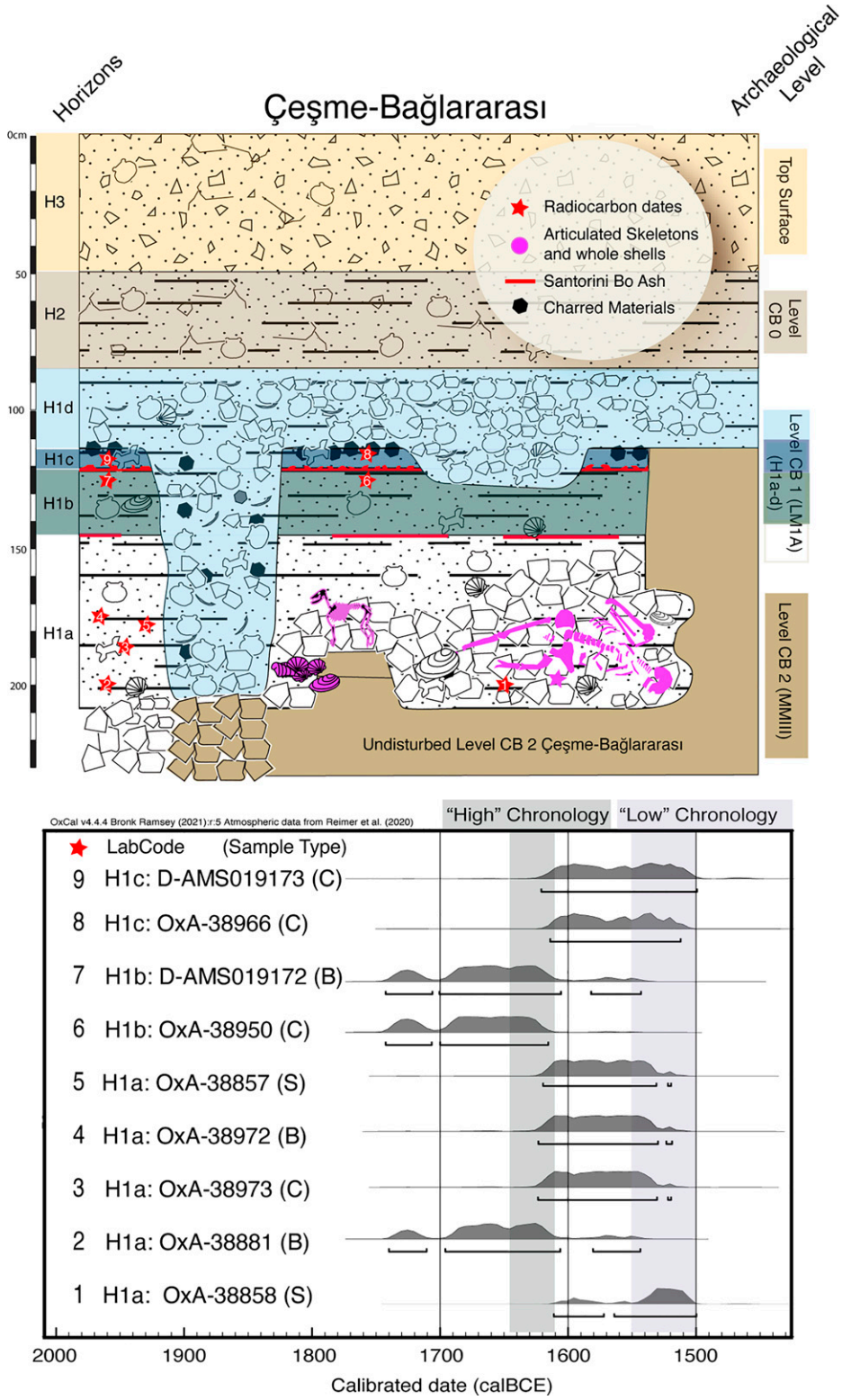

Fig. 3. Illustrated schematic of Çeşme-Bağlararası's stratigraphic sequence, highlighted features, and radiocarbon ages. C, S, and B are used to indicate charcoal, seed, or bone (*SI Appendix*, Table S1). The human and dog skeletons and shell-rich, muddy rip-clast bundle (H1a) are marked in purple. Horizons H1a through d all relate to the Thera eruption event but represent four consecutive but time-separated tsunami wave inundations. The intruding sediments from H1d were the result of the salvaging of building stones (deeper pit) and possibly rescue efforts (shallower pits) during a hiatus in tsunami arrivals. H2 is a later archaeological deposit that accumulated over time. H3 includes upper agricultural and top surface soils.

individuals/cm^3 and 2.9 species/cm^3 with a high proportion of staining (Fig. 4 and Dataset S1). All >500-μm samples included fragmented, whole-shell, and urchin spicula (combined total average 12.2/cm^3). Elemental values (X-ray fluorescence spectroscopy [XRF]; Dataset S1) in H1 relative to H2 and H3 are higher in Ca and lower in Al. The lower subhorizons H1a

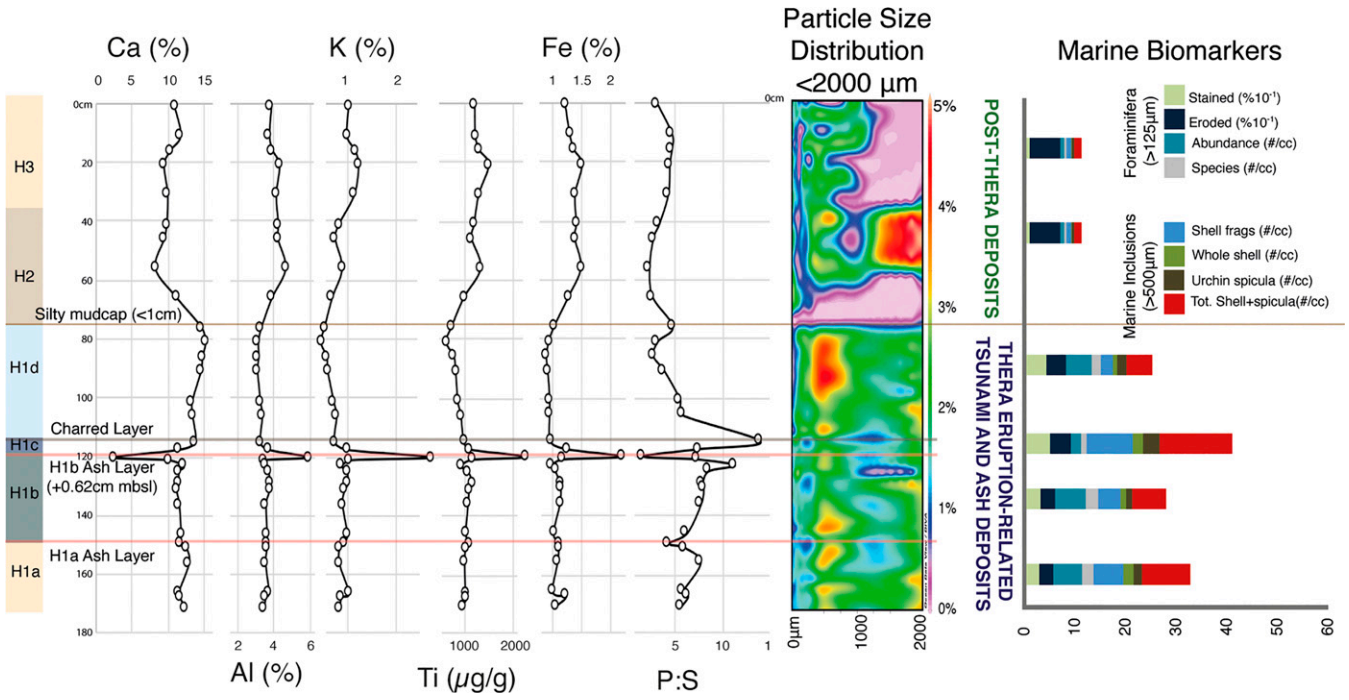

Fig. 4. Results of multiproxy analysis of sediment section outside of fortification walls. Elemental values (XRF), grain size distribution, and marine biomarkers from sedimentological section (Dataset S1) are shown with interpreted differentiation of layers. Ash layer is located at +0.62 cm mbsl. Contour grid of grain size data produced using Ocean Data View (60).

through c have slightly lower values of Ca and higher values of Al than H1d. The more prominent, ash layer at the top of H1b shows high peaks in Ti, Al, K, Fe, Si, and relatively lower values in Ca (Fig. 4 and Dataset S1). P:S values peak in the bone-rich charred layer (top of H1c) and fall in the ash layer (top of H1b). H1 includes Late Minoan IA pottery (CB Level 1).

H2 (Figs. 3 and 4) contains archaeologically rich deposits with CB Level 0 pottery including Mycenean types (29) and root casts. Marine markers are lower than H1 (avg. 1.7/cm^3). H3 contains living roots and mixed pottery from many phases including late Roman/Byzantine period. Some minor fluctuations are present in the uppermost exposed surface. The foraminifera abundance in layers H2 and H3 range from one to two individuals per cubic centimeter, all of which are eroded and lack signs of staining.

Archaeological Excavations. The lower rubble layer (H1a) was laterally extensive (30) (Fig. 2 and *SI Appendix*, Figs. S2–S4), abutted the fortification walls, and also intruded into the buildings. It included pottery, shell, bone, and charcoal and was dominated by stones similar to the adjacent structures. Late Minoan IA pottery, some of which was imbricated, and other archaeological artifact-rich sediments overlay the rubble. A patch (~40-m diameter) of *Cerastaderma glaucum* and *Patella sp.* shells within a muddy ripclast were wedged against a wall (Fig. 3 and *SI Appendix*, Fig. S1). Nearby, an articulated dog skeleton was found in an entryway beneath collapsed stones (Figs. 3 and 5). The corner of another room failed inward (*SI Appendix*, Figs. S2 and S3), and the incoming rubble spill was covered by a darker, silty sediment. Within a distance of a few meters from the collapsed and damaged area, structures were undamaged with intact pathways and walls. The contact between the disrupted area and the intact side was lenticular and abrupt with a scalloped shape (Fig. 3 and *SI Appendix*, Figs. S3 and S4).

An articulated young adult male human skeleton was found within the rubble in a prone, slightly curved position following the curvature of this contact (Figs. 2, 3, and 5 and *SI Appendix*, Fig. S4). The skeleton did not have any signs of deliberate, culturally appropriate burial (e.g., positioning, grave goods, context, and treatment).

Pits were found throughout these ruins, some with the clear purpose of extracting building stones from underlying structures and others with no apparent function (Fig. 3 and *SI Appendix*, Figs. S2–S4).

Discussion

Signs of Tsunamis. The archaeological and sedimentological results from H1 horizon include ample indicators known from modern and paleotsunami deposits including allochtonous marine inclusions (31, 32) (Figs. 3–5), higher foraminifera abundance with staining (33), elemental trends skewed toward marine-like values, imbrication (34), collapsed structures (and related rubble layers), and nondeliberate burials.

C. glaucum, found in a patch at the excavation, are brackish water clams that live in highly concentrated beds (35). This muddy clast of shells was probably entrained, transported, and rafted until it was lodged against the building. *Pattelae sp.* marine limpet mollusks were also identified among the rubble. This species attaches itself to hard surfaces, such as rocky coasts or marine structures (36), and similarly could have arrived during the tsunami. Whole, articulated domesticated animal skeletons in nonrefuse and nonburial context such as the dog found near the shelly patches is also a tsunami marker (37, 38).

There are signs of collapse and intrusion into the buildings that does not fit earthquake evidence, because the damage is unidirectional, and adjacent and nearby walls are unaffected (39). For example, in one of the houses connected to the fortification walls (40), a rubble layer intrudes from a collapsed portion of the wall and is blanketed by a darker soil that continues even further into the room (Fig. 3 and *SI Appendix*, Fig. S2). Such deposits would have required a very strong force to

Fig. 5. Tsunami rubble with articulated skeletal remains (*Right*). Articulated human skeleton (*Top Left*), articulated dog skeleton, and shell-rich muddy patch (*Bottom Left*) were present within the debris.

dismantle and redistribute the stones. The rubble at the base of the horizons (H1a) includes some very large clasts, in general ranging from ∼25 to 40 cm, framework-supported with silty sediments in the cavities. The last of the tsunami-related horizons (H1d) is also rich with rubble, though the clasts are more similar to one another in size and do not exceed about 15 cm at their longest axis.

The articulated young male human skeleton exhibits classic signatures of deposition within debris flow. The location of the skeleton faces the most severely damaged portion of the fortification wall (*SI Appendix*, Fig. S4), suggesting the wall's failure point at the time of the event. A radiocarbon age measurement from a charred piece of *Hordeum vulgare* nearest to the skeleton within this same deposit gives the youngest range of age results among all of the measurements (Fig. 3 and *SI Appendix*, Figs. S6 and S7 and Table S1), fitting more with the "low" rather than "high" chronology.

Searching for the Injured and Missing. After a natural disaster such as a tsunami, survivors are tasked with the responsibility of rescuing victims, recovering the dead, caring for the injured, and post-event clean-up. At Çeşme-Bağlararası this effort is visible in the presence of misshapen pits, interpreted here as the preserved remains from their effort to retrieve victims from the tsunami debris. The human skeleton was located about a meter below such a pit, suggesting that it was too deep to be found and retrieved and therefore (probably unknowingly) left behind. It is also in the lowest part of the deposit, characterized throughout the debris field by the largest and heaviest stones (some larger than 40 cm in diameter; Figs. 3 and 5 and *SI Appendix*, Figs. S1 and S4), further complicating any retrieval effort.

In both the 2004 Indian Ocean Tsunami and the 2011 Tohoku Earthquake tsunami, missing persons accounted for over 10% of the dead even a decade after the events (41, 42). Victims that are swept up in the debris flow during a tsunami can get deeply buried within it or drown at sea, thereby making 100% victim recovery unrealistic. The Çeşme-Bağlararası young man is an ancient example of the same phenomenon.

The Age of the Eruption and Tsunamis. All radiocarbon ages have two sigma (95%) time ranges that coincide with both the high and low chronologies for the LBA Thera eruption and tsunami events (H1a-d; Figs. 3 and 4 and *SI Appendix*, Figs. S6 and S7 and Table S1). However, the samples also group into two clusters, one which encompasses more of the "low" range and the other the "high" range, although this clustering has no association with stratigraphic position. The significance of this is that there is no age gradient by depth. H1a contains ages trending to both high and low chronologies, H1b (above H1a) contains high chronology trending ages, and H1c includes low chronology trending ages. This lack of chronological gradient associated to each tsunami horizon agrees with known tsunami sediment–related age mixing (38). We suggest that because all of the samples are from a well-sealed but heavily mixed (tsunami) context, the youngest ages are more relevant for determining the age that is closest to the event itself. Thus, a wide range of ages are expected and even diagnostic as evidence for tsunami deposition, due to their chaotic nature. According to this principle, the entire event deposit (H1a through d) cannot be older than the youngest measurement (terminus post quem) within it. The bimodal nature of the two clusters may reflect the mixing from the underlying archaeological settlement, which is an older, out-of-use portion of the site, with younger materials arriving from more recently active areas of the settlement. Accordingly, the two sigma (95%) radiocarbon age results of the sample closest to the human skeleton (OxA-38858; Cal BCE 1612 to 1573 [19.4%] and Cal BCE 1565 to 1501 [76.1%]) would be the most representative of the event's age. While these ages do not negate either chronology, it does limit the age to no older than1612 BCE and includes ample support for the low chronology. The calibration within this time period is notoriously problematic and has long been the subject of extensive research (19, 21, 24, 43–45). While the dates presented here do not definitively resolve the issue, they do provide fresh radiocarbon data from a well-sealed, archaeologically associated, Theran eruption-related event horizon in the Aegean and will likely open discussion.

The Sequence of Events Related to the Eruption of Santorini, as Seen from Çeşme-Bağlararası. We propose that at the western Anatolian/Aegean site of Çeşme-Bağlararası, the eruption of Thera volcano produced a series of tsunami landfalls that

arrived at the semiclosed Bay of Çeşme (*SI Appendix*, Fig. S8). There are four discernible horizons identified, though more could be present. Here, we will address those that are clearly apparent. In the first tsunami ("H1a"), portions of the structures in the water's path failed, and those stones were strewn across the area. In some cases, walls (perhaps sections which already exhibited weaker failure points) tumbled into building interiors, carrying debris and construction materials as well as unfortunate victims. "Çeşme Man," the well-preserved articulated skeleton within this tsunami layer, represents the only preserved human remains identified in deposits associated with the LBA eruption of Thera.

After a short hiatus (a few hours), during which tephra accumulated, a second tsunami arrived (H1a/H1b contact), possibly associated to the same eruption phase. Following this second tsunami, a longer period of quiet occurred, allowing the ash to accumulate on top of the tsunami debris (H1b/H1c interface). Meanwhile, fires were actively burning throughout the Aegean (terrestrial and marine) as the ash fell, and burning materials floated at sea. After the hiatus following H1b, a third, smaller, tsunami incursion delivered a package of sediments and charred or still-burning materials ("H1c"). The flame-up structures present at the top of the ash layer between H1b and H1c occur at the interface of lower- and higher-density deposits, either due to liquefaction or water erosion, and has been reported in both modern and ancient tsunami deposits (46, 47). The truncation of the flame structures occurs as the sediment-dense water flow traverses the surface. The H1c tsunami deposit is similar to H1b but lacks the concentrated ash layer at its top and is instead capped with charred materials (e.g., bone and vegetation), a portion imbricated or laying horizontally.

After the third tsunami (H1c), we suspect that there was a longer (days to weeks) quiescence in event activity, during which people began to search for human remains and collect materials for repairs or new construction. Unfortunately for them, this period ended, as another tsunami arrived, of similar magnitude to the first tsunami, and left another thick deposit over the already damaged area, including filling the recently dug pits and stone-removal sections (Fig. 2). This entire sequence is presumed to have occurred in a matter of days or weeks.

The absence of ash at the surface of H1c might be explained by a few possibilities. One possibility is that ash fallout ended due to the exhaustion of its supply, indicating a time gap from the initial high, atmospheric, ash-extruding Plinian eruption ("Phase 1/Bo1") or a shift in wind direction. A third possibility is that the layer was initially deposited but then did not preserve, because it was eroded away or otherwise disrupted, especially in the case of victim retrieval and reconstruction activities.

H1c is followed by another tsunami deposit (H1d). H1d has larger inclusions and is a thicker deposit (~35 cm versus ~6 cm), suggesting a stronger tsunami than H1c, though smaller than the lower tsunami sediment package (H1a and H1b >80 cm). The upper horizons (H2 and H3) fit typical near-coastal terrestrial values with regard to all proxies and lack the aforementioned tsunami-linked structural features (e.g., imbrication, erosional contacts, truncated flame structures, etc.).

The identification of multiple tsunami events at Çeşme-Bağlararası supports the proposed view that there were distinctive eruption phases, with varying hiatuses between them (5, 15, 48). While many tsunami scenarios concentrate attention toward the southern or southeastern directions (5) or near-field along the outskirts of the island itself (15), some simulations include as far north as Çeşme (49). This is evidence that supports that model.

Compound Disaster. Following the event, according to the archaeological remains, the thriving community at Çeşme-Bağlararası ceases to exist for at least a century. In addition to loss of life and property damage, any coastal features or harboring areas would have been debris strewn and made unusable or highly compromised for a period, and the ash deposits would have altered the chemistry of the soils, impacted aquifers, and damaged crops (3).

Çeşme-Bağlararası is only one of many coastal settlements impacted by the eruption and related earthquakes, tsunamis, ashfall, and fires and will provide a type site reference for identifying others. Despite this presumed regional impact, tsunami evidence has only been reported for a handful of sites; namely Malia (50), Letoon (51), Palaikastros (52), Gouves, Didim, and Fethiye (53) (Fig. 1). We argue that this dearth of reports is an artifact of methodological approach wherein 1) the ability to identify paleotsunami sediments has advanced in recent years, and 2) sites lacking tephra were usually not considered for tsunami deposits. Although prevailing winds direct the ash cloud, the tsunami waves are propagated in a linear, concentric pattern to large distances, provided there is no obstacle (islands and peninsulas), in which case, the wave energy will bend, interfering and reflecting off of one another, resulting in either increased or decreased wave heights and coastal inundation (49). Tsunamis, unlike tephra fallout, are independent of wind patterns. Therefore, even in the absence of ash fallout, in areas such as the western Aegean coastlines, tsunami deposits may be present but not yet recognized.

Sea-borne trade at the time of the event was central to the vitality and power of societies, in particular the sea-dominating Minoans. The social fallout from the destruction of the system's core infrastructure (ships, harbors, ports, and coastal settlements) cannot be understated. While many people survived the event, the dynamics of everyday life, political relationships, and economic structures would have shifted.

Disasters and the human reaction to them alter societies. In the case of the LBA eruption, it can be considered a compound disaster wherein multiple short-term (loss of life and property, settlement destruction, economic destabilization, and emigration) and long-term challenges (crop loss and demographic and trade network shifts) necessitated societal responses that would have had a multigenerational impact. While many people survived the event, their worlds would have changed. Çeşme Man is a representative of the many people who died or went missing on that tragic day and did not live to witness perhaps one of humanity's most triumphant revivals.

Materials and Methods

Instrumental neutron activation analysis was conducted by Max Bichler and Johannes Sterba following protocols from (54, 55). Nearby samples from Chios were used for comparison as well as published data. An amount of 500 g of the ash band as provided was investigated for its chemical composition by neutron activation analysis. For the ash layer, contamination by sediments and organic material were visible. To separate a clean sample, the ash was treated twice with 500 mL of HNO_3 (1.4 M, suprapure) for acidic decarbonatization.

After filtering and washing, the sample was then fractionated by particle size by repeated suspension in distilled water. After 1 min of sedimentation time, the liquid was decanted and the process repeated until the liquid appeared clear. The remaining material was then, after drying with acetone, sieved to separate a fine fraction with a diameter of <0.5 mm.

Investigation of this fine fraction under a dual polarizing microscope showed an almost-pure glass fraction. Throughout the cleaning and sedimentation process, a total of eight single pieces of pumice (all less than 1 mm in diameter) were separated by flotation.

After sample processing, ~100 mg of the two separated fractions (fine and remainder) as well as all single pieces of pumice were weighed into Suprasil quartz glass vials and irradiated together with international certified reference materials CANMET reference soil SO1, NIST SRM 1633b Coal Fly Ash, BCR No. 142 light sandy soil, NIST SRM 2702 Inorganics in Marine Sediments, and the MC rhyolithe GBW 07113 for 35 h in the TRIGA Mk II reactor of the TRIGA Center Atominstitut in Vienna at a neutron flux density of $1{\cdot}10^{13}/cm^{-2}/s^{-1}$. After irradiation, sample vials were decontaminated on the outside and measured twice after a cooling time of 5 d and 28 d, respectively. Measurement times on the high purity germanium radiation detector (1.78-keV resolution at the 1,332-keV ^{60}Co peak; 48.2% relative efficiency) were 1,800 s and 10,000 s. Gamma spectra were evaluated using the Genie 2000 software, and by

comparison with the reference materials, elemental concentrations for the elements Na, K, Sc, Cr, Fe, Co, Zn, As, Rb, Zr, Sb, Cs, Ba, La, Ce, Nd, Sm, Eu, Tb, Yb, Lu, Hf, Ta, Th, and U were calculated.

XRF methods followed Zirks et al., 2021 (56). Grain size measurement protocols followed Goodman-Tchernov et al., 2009 (4). Radiocarbon samples were measured at Direct AMS (Washington) and The Oxford Radiocarbon Accelerator Unit.

For marine bioindicators, 2.5 cm^3 of each sediment section were sieved at 63-, 125-, and 500-μm mesh-sized sieves. Each sample was assessed under a binocular microscope and described for general characteristics, mineral content, and inclusions. Foraminifera (125 μm +) were counted and described with regard to taphonomic condition (33). Species were presumed based on morphological uniqueness and similarity, but not all were identified. Inclusions of urchin spines (bases), shell fragments, and whole shell in the 500+-μm fraction of each sample were quantified by individual pieces.

Data Availability. All study data are included in the article and/or supporting information.

ACKNOWLEDGMENTS. Çeşme-Bağlararası excavations have been conducted under permits and with funding support from the Ministry of Culture and Tourism, Turkey. Activities occurred within the course of the Izmir Region Excavations and Research Project under the framework of Ankara University Mustafa V. Koç Research Center for Maritime Archaeology (ankusam.ankara.edu.tr). Additional funding for the research has been provided by The Scientific and Technological Research Council of Turkey Project 108K263, 114K266 (V.Ş., H.E.), Institute for Aegean Prehistory: INSTAP (V.Ş., H.E.), Ankara University Rectorates (V.Ş., H.E.), Ankara University Faculty of Languages, History and Geography (V.Ş.), Institute for Aegean Prehistory Study Center for East Crete (V.Ş.), Çeşme Municipality (V.Ş., H.E.), Urla Municipality (H.E.), İzmir Metropolitan Municipality (V.Ş., H.E.), Turkish Historical Society (V.Ş.), Koç Foundation (H.E.), Turkish Institute of Nautical Archaeology (V.Ş., H.E.), Israel Science Foundation ISF 984-10 (B.N.G.-T.), Sir Mick Davis (B.N.G.-T.), Norman Krischer (B.N.G.-T.), Tzili Charney (B.N.G.-T.), and National Geographic Grant (B.N.G.-T.). Field observations, laboratory assistance, remarks, and feedback are from Rıza Tuncel, Evangelia Kiriatzi, Mustafa İncirlili, Yılmaz S. Erdal, Henry P. Schwarcz, Dan Tchernov, Joy Kroin, Joe Boyce, Douglas Faulmann, Kirki, Mjr. Tom, and Paul Falkowski. Special appreciation goes to the four anonymous reviewers who provided excellent insight and greatly improved the final manuscript.

1. C. Doumas ed., Thera and the Aegean World II: Papers and Proceedings of the Second International Scientific Congress (The Thera Foundation, Santorini, Greece, 1980).
2. C. Doumas, L. Papazoglou, Santorini tephra from Rhodes. *Nature* **287**, 322–324 (1980).
3. J. Driessen, C. F. Macdonald, *The Troubled Island. Minoan Crete Before and after the Santorini Eruption* (Liège & Austin, 1997).
4. B. N. Goodman-Tchernov, H. W. Dey, E. G. Reinhardt, F. McCoy, Y. Mart, Tsunami waves generated by the Santorini eruption reached Eastern Mediterranean shores. *Geology* **37**, 943–946 (2009).
5. F. W. McCoy, G. Heiken, Tsunami generated by the Late Bronze Age eruption of Thera (Santorini), Greece. *Pure Appl. Geophys.* **157**, 1227–1256 (2000).
6. G. Zanchetta *et al.*, Tephrostratigraphy, chronology and climatic events of the Mediterranean basin during the Holocene: An overview. *Holocene* **21**, 33–52 (2011).
7. C. U. Hammer, H. B. Clausen, W. Dansgaard, Greenland ice sheet evidence of postglacial volcanism and its climatic impact. *Nature* **288**, 230–235 (1980).
8. V. C. LaMarche, K. K. Hirschboeck, Frost rings in trees as records of major volcanic eruptions. *Nature* **307**, 121–126 (1984).
9. M. W. Salzer, M. K. Hughes, Bristlecone pine tree rings and volcanic eruptions over the last 5000 yr. *Quat. Res.* **67**, 57–68 (2007).
10. J. Driessen, The Santorini eruption. An archaeological investigation of its distal impacts on Minoan Crete. *Quat. Int.* **499**, 195–204 (2019).
11. J. Keller, "Quaternary tephrochronology in the Mediterranean region" in *Tephra Studies*, S. Self, R.S.J. Sparks, Eds. (Springer, Dordrecht, The Netherlands, 1981).
12. A. Vinci, Distribution and chemical composition of tephra layers from Eastern Mediterranean abyssal sediments. *Mar. Geol.* **64**, 143–155 (1985).
13. C. Doumas, *Thera: Pompeii of the Ancient Aegean* (Thames & Hudson, London, UK, 1983).
14. K. J. Evans, F. W. McCoy, Precursory eruptive activity and implied cultural responses to the Late Bronze Age (LBA) eruption of Thera (Santorini, Greece). *J. Volcanol. Geotherm. Res.* **397**, 106868 (2020).
15. P. Nomikou *et al.*, Post-eruptive flooding of Santorini caldera and implications for tsunami generation. *Nat. Commun.* **7**, 1–10 (2016).
16. J. S. Soles, "The impact of the Minoan eruption of Santorini on Mochlos" in *Times Up! Dating the Minoan Eruption of Santorini*, D. A. Warburton, Ed. (Monographs, 2009), pp. 107–116.
17. S. Marinatos, The volcanic destruction of Minoan Crete. *Antiquity* **13**, 339–425 (1939).
18. P. Warren, V. Hankey, *Aegean Bronze Age Chronology* (Bristol Classical Press, 1989).
19. M. H. Wiener, "Dating the Theran eruption: Archaeological science versus nonsense science" in *Israel's Exodus in Transdisciplinary Perspective: Text, Archaeology, Culture, and Geoscience*, T. E. Levy, T. Schneider, W. H. C. Propp, Eds. (Springer International Publishing, Cham, Switzerland, 2015), pp. 131–143.
20. S. W. Manning *et al.*, Radiocarbon offsets and old world chronology as relevant to Mesopotamia, Egypt, Anatolia and Thera (Santorini). *Sci. Rep.* **10**, 1–14 (2020).
21. R. Friedrich *et al.*, A new annual C dataset for calibrating the Thera eruption. *Radiocarbon* **62**, 953–961 (2020).
22. S. W. Manning, *A Test of Time and a Test of Time Revisited* (Oxbow Books, Oxford, 2014).
23. W. Kutschera, On the enigma of dating the Minoan eruption of Santorini. *Proc. Natl. Acad. Sci. U.S.A.* **117**, 8677–8679 (2020).
24. S. W. Manning *et al.*, Dating the Thera (Santorini) eruption: Archaeological and scientific evidence supporting a high chronology. *Antiquity* **88**, 1164–1179 (2014).
25. V. Şahoğlu, "Çeşme–Bağlararası: A new excavation in Western Anatolia" in Middle Helladic Pottery and Synchronisms: Proceedings of the International Workshop Held at Salzburg, October 31st – November 2nd, 2004, F. Felten, W. Gauss, S. Rudolfine, Eds. (Verlag derÖsterreichische Akademie der Wissenschaften, Wien, Austria, 2007), pp. 309–322.
26. V. Şahoğlu, "Çeşme – Bağlararası: A Western Anatolian harbour settlement at the beginning of the Late Bronze Age" in *NOSTOI: Indigenous Culture, Migration and Integration in the Aegean Islands and Western Anatolia during the Late Bronze Age and Early Iron Age*, N. Stampolidis, Ç. Maner, K. Kopanias, Eds. (Koç University Press, Istanbul, Turkey, 2015), pp. 593–608.
27. S. Vardar, E. Öner, R. İlhan, Bağlararası Höyügü Çevresinde Paleocoğrafya ve Jeoarkeoloji Araştırmaları (Çesme-İzmir). *Türkiye Jeol Bülteni* **60**, 589–614 (2017).
28. P. Stocchi, G. Spada, Glacio and hydro-isostasy in the Mediterranean Sea: Clark's zones and role of remote ice sheets. *Ann. Geophys.* **50**, 741–761 (2007).
29. A. Aykurt, Late Bronze Age pottery from Çeşme Bağlararasi. *Olba* **18**, 1–63 (2010).
30. V. Şahoğlu, "Çeşme–Bağlararası" *Dil ve Tarih Coğrafya Fakültesi 75 Yıl Armağanı Arkeoloji Bölümü Tarihçesi ve Kazıları (1936-2011)*, O. Bingöl, A. Öztan, H. Taşkıran, Eds. (Ankara University Press, 2012), pp. 83–90 .
31. S. V. Donato, E. G. Reinhardt, J. I. Boyce, R. Rothaus, T. Vosmer, Identifying tsunami deposits using bivalve shell taphonomy. *Geology* **36**, 199–202 (2008).
32. E. G. Reinhardt *et al.*, The tsunami of 13 December A.D. 115 and the destruction of Herod the Great's harbor at Caesarea Maritima, Israel. *Geology* **34**, 1061–1064 (2006).
33. J. E. Pilarczyk *et al.*, Microfossils from coastal environments as indicators of paleoearthquakes, tsunamis and storms. *Palaeogeogr. Palaeoclimatol. Palaeoecol.* **413**, 144–157 (2014).
34. R. Paris *et al.*, Boulder and fine sediment transport and deposition by the 2004 tsunami in Lhok Nga (western Banda Aceh, Sumatra, Indonesia): A coupled offshore-onshore model. *Mar. Geol.* **268**, 43–54 (2010).
35. P. Russell, G. Petersen, The use of ecological data in the elucidation of some shallow water European Cardium species. *Malacologia* **14**, 223–232 (1973).
36. D. Vafidis, I. Drosou, K. Dimitriou, D. Klaoudatos, Population characteristics of the Limpet Patella caerulea (Linnaeus, 1758) in Eastern Mediterranean (Central Greece). *Water* **12**, 1186 (2020).
37. B. N. Goodman-Tchernov, "Archaeological dating of tsunami and storm deposits" in *Geological Records of Tsunamis and Other Extreme Waves*, M. Engel, J. Pilarczyk, S. M. May, D. Brill, E. Garrett, Eds. (Elsevier, 2020), pp. 729–739.
38. J. Goff, C. Chagué-Goff, S. Nichol, B. Jaffe, D. Dominey-Howes, Progress in palaeotsunami research. *Sediment. Geol.* **243–244**, 70–88 (2012).
39. J. Lario, T. Bardají, P. G. Silva, C. Zazo, J. L. Goy, Improving the coastal record of tsunamis in the ESI-07 scale: Tsunami Environmental Effects Scale (TEE-16 scale). *Geol. Acta* **14**, 179–193 (2016).
40. V. Şahoğlu, H. Erkanal, Ü. Çayır, Y. Erbil, Çeşme – Bağlararası 2010 Yılı Kazıları. *KST* **33**, 489–508 (2012).
41. NOAA NCEI, *National Geophysical Data Center/World Data Service: NCEI/WDS Global Historical Tsunami Database* (NOAA National Centers for Environmental Information, 2021).
42. N. Yun, M. Hamada, A comparative study on human impacts caused by the 2011 Great East Japan Earthquake and disaster mitigation" in *Proceedings of the International Symposium on Engineering: Lessons Learned from the 2011 Great East Japan Earthquake* (Pacific Earthquake Engineering Research Center, Berkeley, CA, 2012), pp.1666–1679.
43. Y. Ehrlich, L. Regev, E. Boaretto, Discovery of annual growth in a modern olive branch based on carbon isotopes and implications for the Bronze Age volcanic eruption of Santorini. *Sci. Rep.* **11**, 1–11 (2021).
44. C. Satow *et al.*, A new contribution to the Late Quaternary tephrostratigraphy of the Mediterranean: Aegean Sea core LC21. *Quat. Sci. Rev.* **117**, 96–112 (2015).
45. S. Wulf *et al.*, Advancing Santorini's tephrostratigraphy: New glass geochemical data and improved marine-terrestrial tephra correlations for the past ~360 kyrs. *Earth Sci. Rev.* **200**, 10.1016/j.earscirev.2019.102964 (2020).
46. D. Matsumoto *et al.*, Truncated flame structures within a deposit of the Indian Ocean Tsunami: Evidence of syn- sedimentary deformation. *Sedimentology* **55**, 1559–1570 (2008).
47. S. Marco, O. Katz, Y. Dray, Historical sand injections on the Mediterranean shore of Israel: Evidence for liquefaction hazard. *Nat. Hazards* **74**, 1449–1459 (2014).
48. A. Bond, R.S.J. Sparks, The Minoan eruption of Santorini, Greece. *J. Geol. Soc. London* **132**, 1–16 (1976).
49. M. T. Pareschi, M. Favalli, E. Boschi, Impact of the Minoan tsunami of Santorini: Simulated scenarios in the Eastern Mediterranean. *Geophys. Res. Lett.* **33**, 1–6 (2006).

50. L. Lespez *et al.*, Discovery of a tsunami deposit from the Bronze Age Santorini eruption at Malia (Crete): impact, chronology, extension. *Sci. Rep.* **11**, 15487 (2021).
51. E. Aydar, A. Çiner, O. Ersoy, E. Écochard, E. G. Fouache, Volcanic ash and tsunami record of the Minoan Late Bronze Age Eruption (Santorini) in a distal setting, southwestern Turkey. *J. Quat. Sci.* **36**, 586–597 (2021).
52. H. J. Bruins *et al.*, Geoarchaeological tsunami deposits at Palaikastro (Crete) and the Late Minoan IA eruption of Santorini. *J. Archaeol. Sci.* **35**, 191–212 (2008).
53. K. Minoura *et al*., Discovery of Minoan tsunami deposits. *Geology* **28**, 59–62 (2000).
54. C. Peltz, P. Schmid, M. Bichler, INAA of Aegaean pumices for the classification of archaeological findings. *J. Radioanal. Nucl. Chem.* **242**, 361–377 (1999).
55. J. H. Sterba, A workflow for neutron activation analysis of archaeological ceramics at the Atominstitut in Vienna, Austria. *J. Radioanal. Nucl. Chem.* **316**, 753–759 (2018).
56. E. Zirks *et al.*, Redox evolution and the development of oxygen minimum zones in the Eastern Mediterranean Levantine basin during the early Holocene. *Geochim. Cosmochim. Acta* **297**, 10.1016/j.gca.2021.01.009 (2021).
57. E. N. Johnston, J. C. Phillips, C. Bonadonna, I. M. Watson, Reconstructing the tephra dispersal pattern from the Bronze Age eruption of Santorini using an advection-diffusion model. *Bull. Volcanol.* **74**, 1485–1507 (2012).
58. H. Huber, M. Bichler, A. Musilek, Identification of Pumice and Volcanic Ash from Archaeological Sites in the Eastern Mediterranean Region using Chemical fingerprinting. *Egypt and the Levant* **13**, 83–105 (2003).
59. C. D. Athanassas, K. Modis, M. C. Alçiçek, K. Theodorakopoulou, Contouring the Cataclysm: A Geographical analysis of the effects of the Minoan Eruption of the Santorini Volcano. *Environ. Archaeol.* **23**, 160–176 (2018).
60. R. Schlitzer, Ocean data view. https://odv.awi.de/. Accessed 1 May 2021.

PNAS
www.pnas.org

Supplementary Information for
Volcanic Ash, Victims, and Tsunami Debris from the Late Bronze Age Thera Eruption discovered at Çeşme-Bağlararası (Turkey)

Vasıf Şahoğlu[1†*]; Johannes H. Sterba[2], Timor Katz[3], Ümit Çayır[4], Ümit Gündoğan[5], Natalia Tyuleneva[6], İrfan Tuğcu[7], Max Bichler[2], Hayat Erkanal[1‡], Beverly N. Goodman-Tchernov[6†*]

Email: bgoodman@univ.haifa.ac.il, sahoglu@ankara.edu.tr

This PDF file includes:

Supplementary text
Figures S1 to S8
Tables S1
SI References

Other supplementary materials for this manuscript include the following:

Datasets S1

Fig. S1.
Volcanic ash layer and related tsunami deposits (H1a-d) at Çeşme–Bağlararası as seen from the baulk wall of the excavation.

Fig. S2.

Çeşme–Bağlararası excavation area photograph from 2010. A) Stone removal pit (filled with H1d); B) Darker soils that overlay tsunami rubble (H1a); C) Rubble spillover into room through collapsed fortification wall; D) Continuation of the same section from which sediment sampling was carried out, E) Intact portion of fortification wall, F) Undisturbed portion of site (Level CB2).

Fig. S3.

Çeşme–Bağlararası excavation photo from 2012. The collapsed and disturbed walls to the right and the truncated damaged walls are visible on the left. The tsunami deposits H1a continued into the buildings on the left side of the image. Irregular pits are visible throughout the excavation area. The rubble outside the fortification walls is visible on the lower right of the photograph.

Fig. S4.

Young male articulated skeleton within tsunami rubble at Çeşme–Bağlararası. The curve of the excavation around the skeleton marks the extent and shape of the deposit (scalloped/lenticular) The uneroded portion to the right of the skeleton in the photo contains undisturbed archaeological stratigraphy from pre-Thera eruption period (Level CB2).

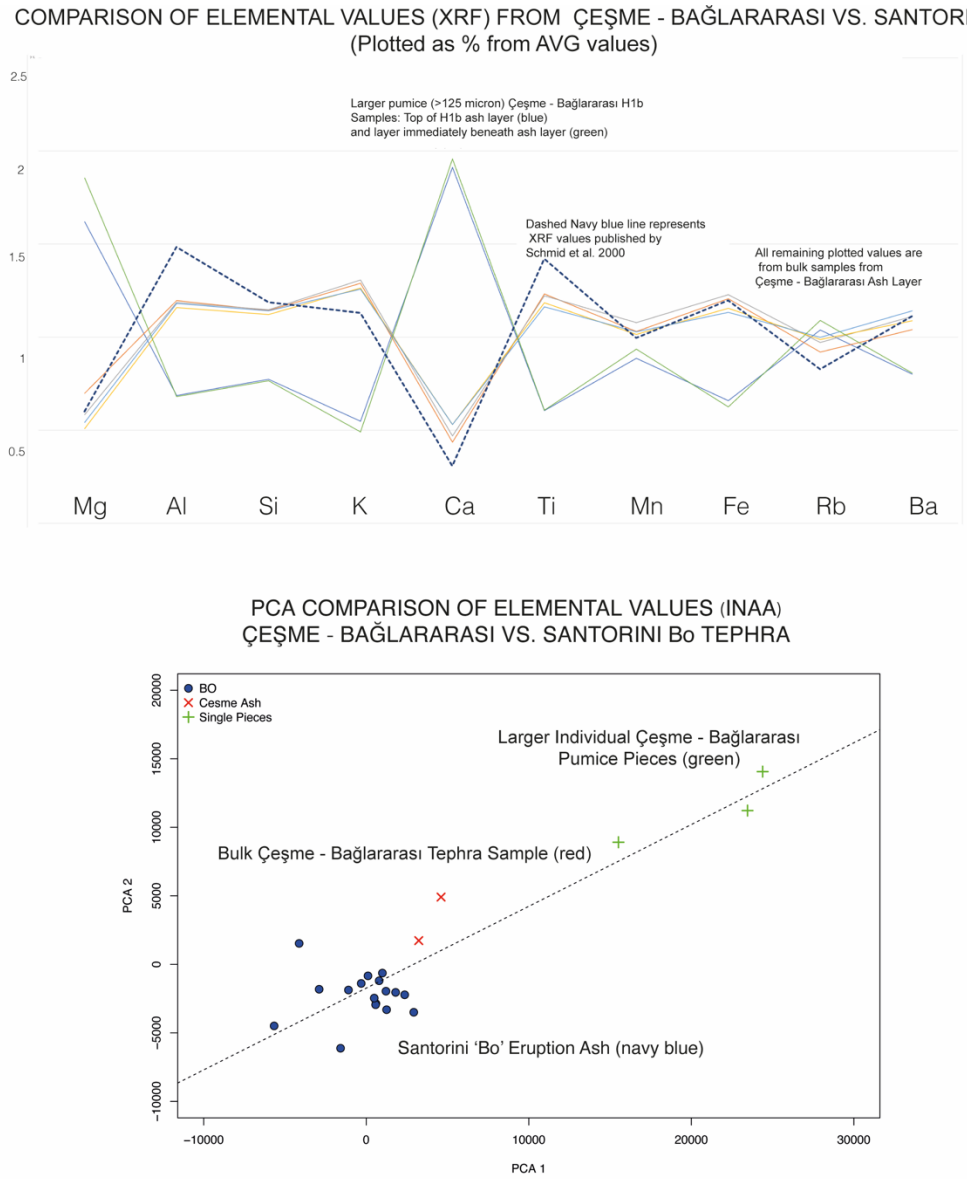

Fig. S5

Upper: Comparison of Elemental Values (XRF) from Çeşme – Bağlararası vs. Santorini.
Lower: PCA Comparison of Elemental Values from Çeşme – Bağlararası vs. Santorini Bo Tephra

Much of Çeşme - Bağlararası's nearby geological deposits are volcanic in origin, resulting in significant amounts of local tephra and pumice within typical background sediments. The identified ash layer is relatively thin, ranging from less than 1 cm to 3 cm thick. The values of the non-sieved ash layer do not perfectly 'match' those of comparative Santorini Bo samples, but instead represent a mixed Bo and older, locally-derived ash and pumice. Other sites in the region, such as Çine Tepecik, Miletos and Iasos, show INAA results that more closely match Bo values. Geographically, relative to Çeşme - Bağlararası, these sites are closer to Santorini, and thus have thicker ash deposits with less mixing with local pumice and ash. Sediment elemental (XRF) values were measured from a coarser fraction (greater than 125 micron, see upper graph) of two samples. The underlying assumption being that due to particle size and distance from Thera these size fractions could not have arrived with the wind, and therefore are of local origin. Results from the larger sized fraction in the ash layer were compared to the results from the larger sized fraction from the underlying non-ash layer (see upper graph). Their similarity supports the

presumption that materials in the coarse fraction are unrelated to the fallout of airborne Theran ash. In the lower graph (INAA), coarse Çeşme - Bağlararası pumices were similarly measured independently and shown to be less similar to Bo samples than the measurements from bulk Çeşme - Bağlararası ash samples. Again, confirming different sources of volcanic ash products within the deposit.

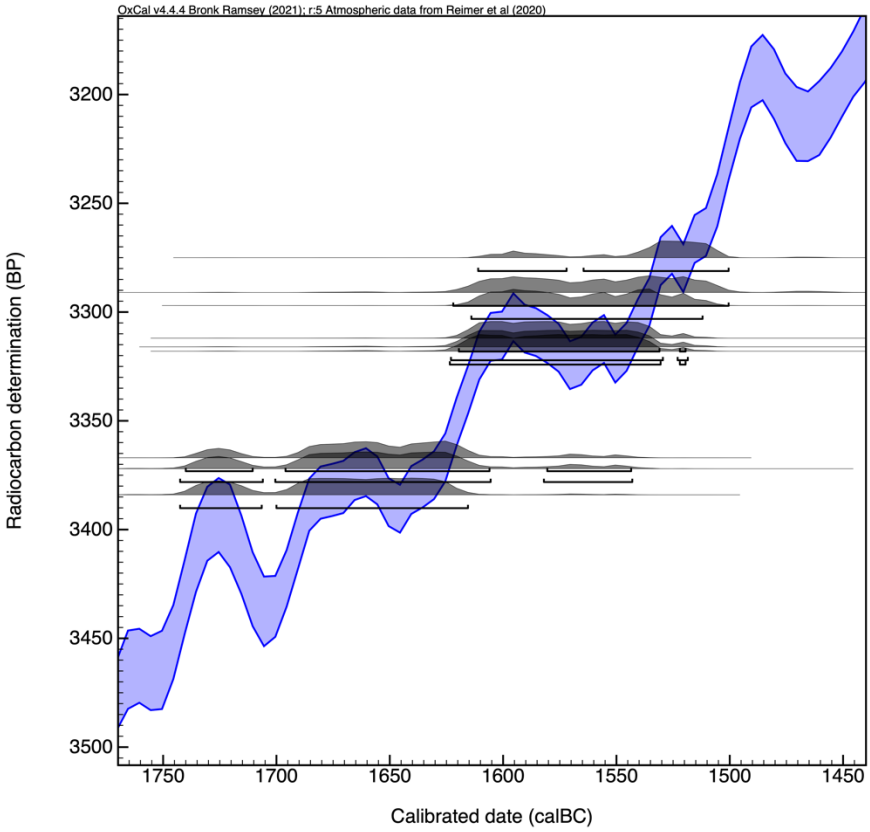

Fig. S6.

All radiocarbon ages calibrated and plotted against the calibration curve. Two clusters are present.

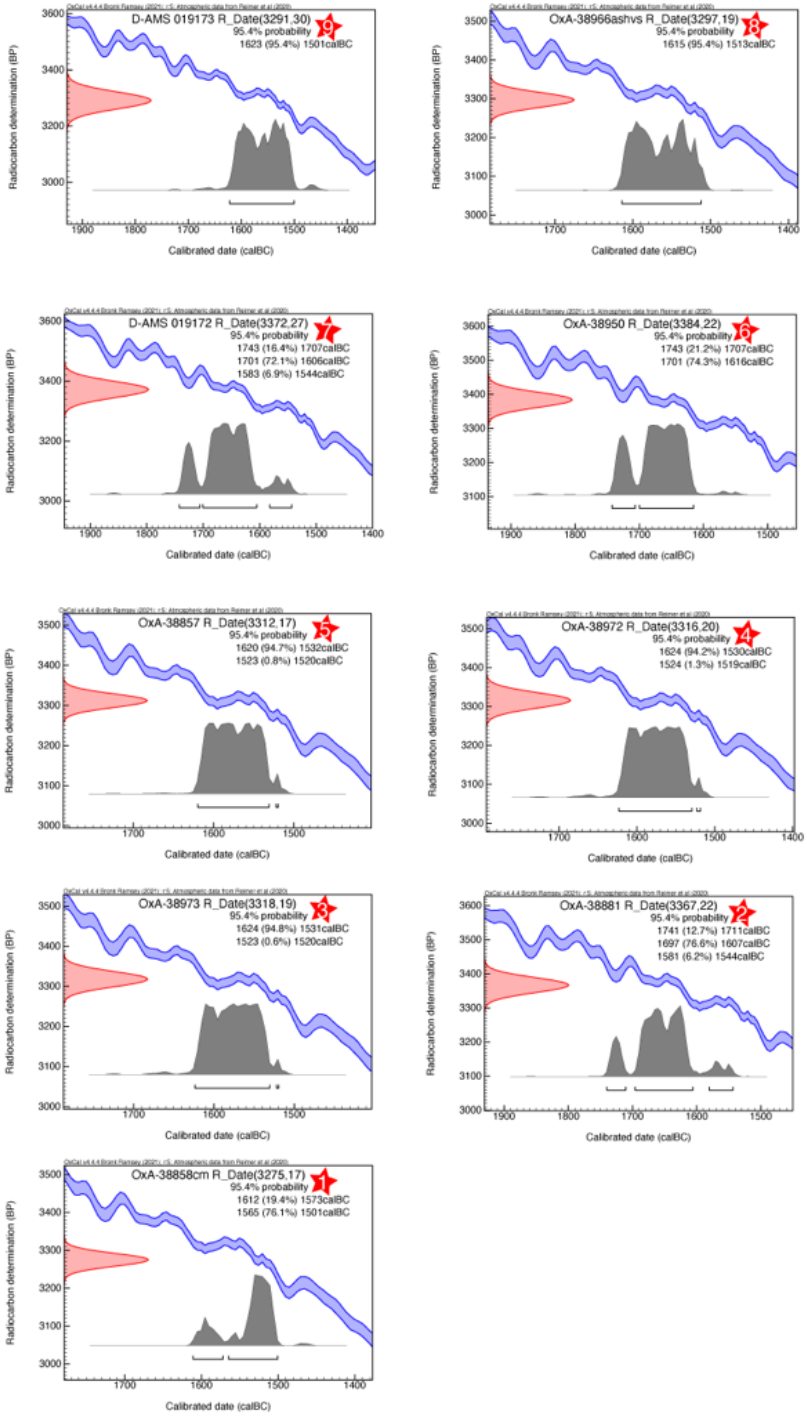

Fig. S7.

OxCal calibrations from individual sample measurements.

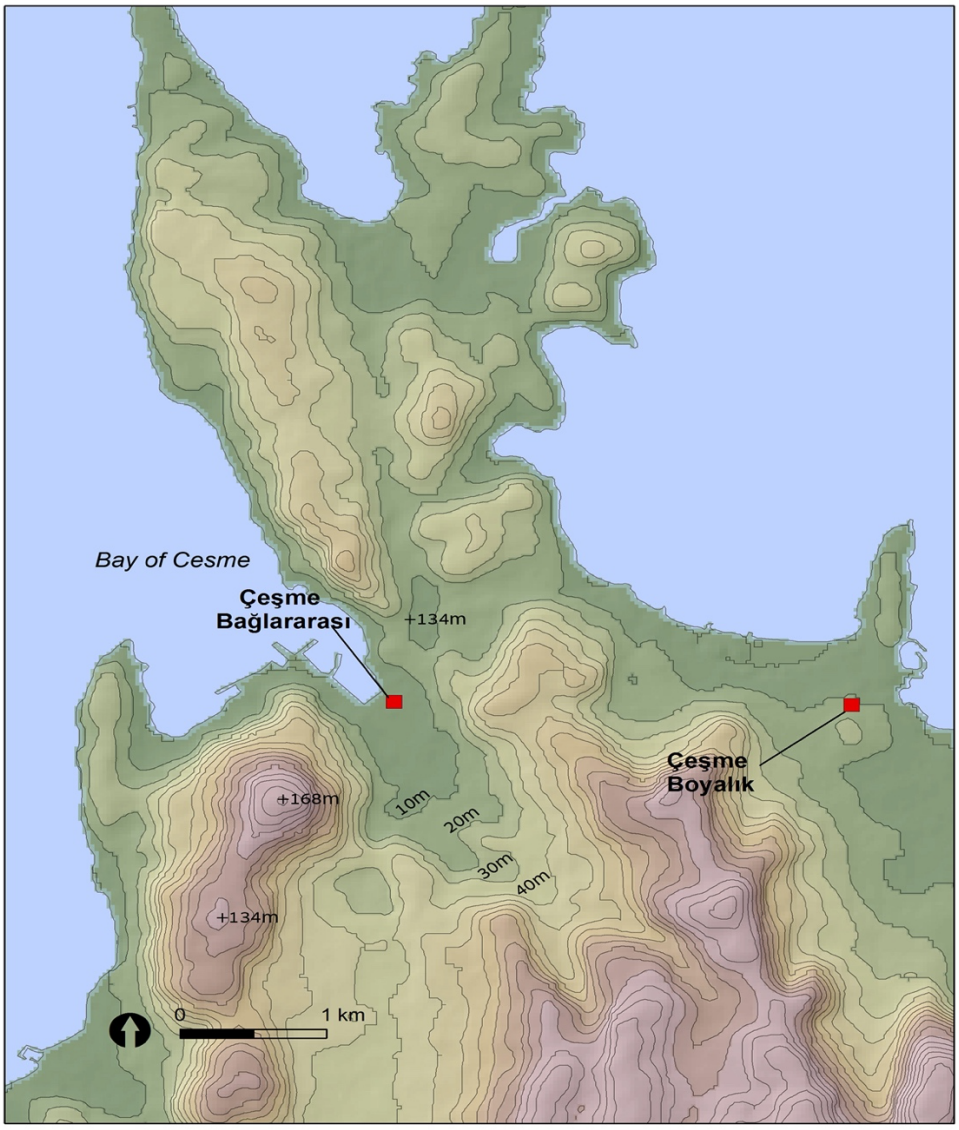

Fig. S8.

Topographic map of Çeşme area and location of Çeşme–Bağlararası site. Isopachs are 10m elevation intervals. Adapted from Şahoğlu 2015 [1], Figure 1, created by Dr. Michele Massa.

Table S1.

Radiocarbon results. Radiocarbon samples were measured at Direct AMS (Washington, USA) and The Oxford Radiocarbon Accelerator Unit (ORAU) and calibrated using OxCal.

LAB ID	Sample # (Fig.3)	LAB	Level	Material	Radiocarbon Date (ybp 1950)	Cal BC/CE MIN (2σ:Oxcal)	Cal BC/CE MAX (2σ:Oxcal)
OxA-38858	1	Oxford	CB 1	*Hordeum Vulgare*	3275±17	1612	1501
OxA-38881	2	Oxford	CB 1	*Bos Taurus*	3367±22	1741	1544
OxA_38973	3	Oxford	CB 1	*Ovis Aries*	3318±19	1624	1520
OxA-38972	4	Oxford	CB 1	*Sus Scrofa*	3316±20	1624	1519
OxA-38857	5	Oxford	CB 1	*Olea europea*	3312±17	1620	1520
OxA-38950	6	Oxford	CB 1	Charcoal	3384±22	1743	1616
D-AMS 019172	7	Direct AMS	CB1	bone (unidentified)	3372±27	1743	1544
OxA-38966	8	Oxford	CB 1	Charcoal	3297±19	1615	1513
D-AMS 019173	9	Direct AMS	CB1	Charcoal	3291±30	1623	1501

Data S1. (separate file)
Table of all sediment analytical results (grain size distribution, XRF, Marine Inclusions) (Excel)

SI References

1. Şahoğlu V (2015) Çeşme – Bağlararası: A Western Anatolian Harbour Settlement at the Beginning of the Late Bronze Age. *NOSTOI: Indigenous Culture, Migration and Integration in the Aegean Islands and Western Anatolia during the Late Bronze Age and Early Iron Age*, eds Stampolidis N, Maner Ç, Kopanias K (Istanbul), pp 593–608.

Sample Code	Horizon inter	Sample Size (	Forams (125+	Stained Forar	Species (#)	#eroded/brol	Shell frags (>	whole shell (>	urchin spines
2	2.5	2	1	2	1	7	0	2
5007		1	0	1	1	3	0	0
10012		3	0	2	2	0	1	3
15017		5	1	2	5	1	2	1
20022		2	0	1	2	4	0	1
25027		4	0	2	3	3	0	0
30032		2	1	1	1	7	0	0
35037		1	0	1	1	5	0	4
40042		5	0	2	4	1	1	0
45047		2	0	2	2	0	1	3
50052		4	1	3	4	0	1	1
55057		1	0	1	1	3	0	0
60062		0	0	0	0	2	1	3
65067		3	0	2	3	6	0	0
70072		2	0	2	2	0	2	0
75077		3	1	2	2	2	0	0
80082		7	2	4	4	3	1	4
85087		18	6	4	5	7	3	9
90092		36	24	7	20	9	6	4
95097		12	9	8	5	12	3	5
100102		13	4	5	6	3	6	8
105107		32	23	7	14	5	0	13
109110		5	2	3	5	5	2	5
110112		16	9	11	10	9	1	3
114116		**6**	5	3	3	14	3	4
116119		8	4	4	5	17	4	7
119122		0	0	0	0	0	0	0
122124		42	20	13	23	14	6	5
124126		14	7	6	4	21	2	8
126128		31	6	15	9	31	1	10
128130		32	7	12	14	4	0	4
130132		6	1	5	2	9	3	0
135137		14	12	4	4	12	6	4
140142		24	9	10	12	26	2	3
143145		8	6	3	6	31	4	8
143145		25	19	11	8	12	8	0
145147		20	7	7	7	13	5	0
147148		33	14	13	15	9	7	7
150152		12	3	5	4	34	8	5
155157		6	5	4	4	6	5	3
160162		41	29	15	13	32	7	3
165167		13	6	6	5	18	9	6
167168		42	16	17	26	11	6	4
170172		2	0	2	0	22	7	7
170174		16	4	5	9	7	4	5
175177		23	4	6	3	31	9	12

Horizon	Normalized	Forams per 1	Stained %	# of species/(	%broken	Shell frags/cc	Whole/cc	urchin spines	TOTAL non-foram/cc
H3		0.8	50.0	0.8	50.0	2.8	0	0.8	3.6
H3		0.4	0.0	0.4	100.0	1.2	0	0	1.2
H3		1.2	0.0	0.8	66.7	0	0.4	1.2	1.6
H3		2	20.0	0.8	100.0	0.4	0.8	0.4	1.6
H3		0.8	0.0	0.4	100.0	1.6	0	0.4	2
H3		1.6	0.0	0.8	75.0	1.2	0	0	1.2
H3		0.8	50.0	0.4	50.0	2.8	0	0	2.8
H3		0.4	0.0	0.4	100.0	2	0	1.6	3.6
H3		2	0.0	0.8	80.0	0.4	0.4	0	0.8
H3		0.8	0.0	0.8	100.0	0	0.4	1.2	1.6
H2		1.6	25.0	1.2	100.0	0	0.4	0.4	0.8
H2		0.4	0.0	0.4	100.0	1.2	0	0	1.2
H2		0	0.0	0	0.0	0.8	0.4	1.2	2.4
H2		1.2	0.0	0.8	100.0	2.4	0	0	2.4
H2		0.8	0.0	0.8	100.0	0	0.8	0	0.8
H2		1.2	33.3	0.8	66.7	0.8	0	0	0.8
H2		2.8	28.6	1.6	57.1	1.2	0.4	1.6	3.2
H1d		7.2	33.3	1.6	27.8	2.8	1.2	3.6	7.6
H1d		14.4	66.7	2.8	55.6	3.6	2.4	1.6	7.6
H1d		4.8	75.0	3.2	41.7	4.8	1.2	2	8
H1d		5.2	30.8	2	46.2	1.2	2.4	3.2	6.8
H1d		12.8	71.9	2.8	43.8	2	0	5.2	7.2
H1d		2	40.0	1.2	100.0	2	0.8	2	4.8
H1d		6.4	56.3	4.4	62.5	3.6	0.4	1.2	5.2
H1c		2.4	83.3	1.2	50.0	5.6	1.2	1.6	8.4
H1c		3.2	50.0	1.6	62.5	6.8	1.6	2.8	11.2
H1b		0	0.0	0	0.0	0	0	0	0
H1b		16.8	47.6	5.2	54.8	5.6	2.4	2	10
H1b		5.6	50.0	2.4	28.6	8.4	0.8	3.2	12.4
H1b		12.4	19.4	6	29.0	12.4	0.4	4	16.8
H1b		12.8	21.9	4.8	43.8	1.6	0	1.6	3.2
H1b		2.4	16.7	2	33.3	3.6	1.2	0	4.8
H1b		5.6	85.7	1.6	28.6	4.8	2.4	1.6	8.8
H1b		9.6	37.5	4	50.0	10.4	0.8	1.2	12.4
H1b		3.2	75.0	1.2	75.0	12.4	1.6	3.2	17.2
H1b		10	76.0	4.4	32.0	4.8	3.2	0	8
H1b		8	35.0	2.8	35.0	5.2	2	0	7.2
H1b		13.2	42.4	5.2	45.5	3.6	2.8	2.8	9.2
H1a		4.8	25.0	2	33.3	13.6	3.2	2	18.8
H1a		2.4	83.3	1.6	66.7	2.4	2	1.2	5.6
H1a		16.4	70.7	6	31.7	12.8	2.8	1.2	16.8
H1a		5.2	46.2	2.4	38.5	7.2	3.6	2.4	13.2
H1a		16.8	38.1	6.8	61.9	4.4	2.4	1.6	8.4
H1a		0.8	0.0	0.8	0.0	8.8	2.8	2.8	14.4
H1a		6.4	25.0	2	56.3	2.8	1.6	2	6.4
H1a		9.2	17.4	2.4	13.0	12.4	3.6	4.8	20.8

	Forams per 1	Stained %	# of species/	%broken	Shell frags/cc	Whole/cc	urchin spines	TOTAL non-foram/cc
H3	1.1	1.2	0.6	8.2	1.2	0.2	0.6	2.0
H2	1.1	1.2	0.8	7.5	0.9	0.3	0.5	1.7
H1d	6.9	5.7	2.4	5.3	3.2	1.2	2.6	7.0
H1c	2.8	6.7	1.4	5.6	12.4	2.8	4.4	19.6
H1b	8.3	4.2	3.3	3.8	6.1	1.5	1.6	9.2
H1a	7.8	3.8	3.0	3.8	8.1	2.8	2.3	13.1
H1	6.4	5.1	2.5	4.6	7.4	2.1	2.7	12.2